Biomedical Signal Processing and Control 86 (2023) 105078

Contents lists available at ScienceDirect

Biomedical Signal Processing and Control

journal homepage: www.elsevier.com/locate/bspc

Knowledge-guided 2.5D CNN for cerebral microbleeds detection

Zhongding Fang [a], Rong Zhang [a,*], Lijun Guo [a], Tianxiang Xia [a], Yingqing Zeng [b], Xiping Wu [c]

[a] Faculty of Electrical Engineering and Computer Science, Ningbo University, Ningbo, Zhejiang, China
[b] The Affiliated Hospital of Medicine School of Ningbo University, Ningbo, Zhejiang, China
[c] Department of Neurology, Ningbo Medical Center Li-Huili Hospital, Ningbo, Zhejiang, China

ARTICLE INFO

Keywords:
Deep learning
Cerebral microbleeds
Priori knowledge
Body plane

ABSTRACT

Cerebral microbleed (CMB) based on magnetic resonance imaging has been recently investigated as key biomarker in the diagnosis of cerebral small-vessel diseases and vascular cognitive impairment. Because the CMB lesions are typically small in size, and easily confused with various analogs such as calcified deposits, artifacts, and especially blood vessels when they are observed from a single MRI slice, reducing false positives in CMB detection is quite challenging. In addition, the lack of available medical image data, which inevitably leads to the imbalance between positive and negative samples, is also a challenge to existing deep learning algorithms. To address these problems, this paper proposes a simple but effective CMB detection method based on a novel deep architecture. First, in contrast to the current local patches-based approach, we make full use of the information about the distribution of CMBs in the whole brain based on training data as priori knowledge to guide the model to obtain candidate CMB patches. Second, we propose a 2.5D convolutional neural network based on morphological differences in cerebral blood vessels and cerebral microbleeds. Specifically, we further use information of the candidates in the coronal and sagittal planes and combine the inference based on three planes to determine the CMB probability of each patch. This approach strikes a balance between the high computational cost and the loss of spatial information. The effectiveness of the proposed method is demonstrated through experimental results that show that our KBPNet model has a sensitivity of 98.24%, an accuracy of 94.10% and an average number of false positives per patient of 1.72 on the SWI-CMB dataset.

1. Introduction

Cerebral microbleeds (CMBs) are hemosiderin depositions caused by cerebral microvascular lesions and typically appear as hypointensity lesions of 2–10 mm in T2-gradient-recalled echo imaging (T2*-GRE) or susceptibility-weighted imaging (SWI) [1]. The CMB prevalence increases with age, reaching 18% among people aged 60 to 69, and 38% among people aged over 80 [2]. At present, CMBs are recognized as biomarkers of small cerebrovascular disease, also known as cerebral small-vessel disease (CSVD) [3–7]. In addition, the CMB spatial distribution highly reflect the spread of different cerebral microvascular diseases. For example, cerebral microbleeds in lobular areas of the brain potentially indicate the occurrence of cerebral amyloid angiopathy [8], while deep subcortical microbleeds indicate hypertensive angiopathy [9]. Moreover, CMBs may be indicative of certain types of cognitive impairment such as Alzheimer's disease [10]. However, manual labeling in clinical examination, even for experienced radiologists, is laborious, time-consuming and error prone [11]. Automatic, timely, and accurate CMB detection can relieve the pressure on radiologists, assist clinicians in diagnosing cerebrovascular disease or assessing the extent of cognitive impairment, and allow early clinical interventions.

Nevertheless, CMB detection is generally quite challenging due to the small size of the CMB lesions. In addition, the confusion of various analogs, such as artifacts, calcification deposits and hypointensity lesions in SWI or T2* imaging, causes a large number of false positives. To improve the CMB detection accuracy and reduce false positive results, most of the existing automatic CMB detection methods adopt a two-step strategy. The first step is a preliminary screening step to find candidate CMBs while the second step is a fine screening step, in which the candidate CMBs are further examined in order to exclude false-positive outcomes. In recent years, the progress of deep learning, especially the development of convolutional neural network (CNN), have promoted the performance of CMB detection methods. Undoubtedly, 3D convolution operation is suitable for extracting brain structure information from continuously scanned brain image sequences. Most notably, Dou et al. [11] proposed a two-step CMB detection method, in which they employed 3D fully convolutional network (FCN) and 3D CNN in the two steps, respectively. However, 3D convolution brings

* Corresponding author.
E-mail address: zhangrong@nbu.edu.cn (R. Zhang).

https://doi.org/10.1016/j.bspc.2023.105078
Received 19 October 2022; Received in revised form 23 April 2023; Accepted 23 May 2023
Available online 12 June 2023

a huge amount of computation. Some hybrid methods have been proposed where 2D and 3D data representations are jointly employed for CMB detection. For instance, Al-Mansi et al. [12] proposed a detection method based on a 2D you-only-look-once (YOLO) architecture and a 3D CNN. However, these heterogeneous two-stage methods need to train different networks in two stages and require a large amount of training data. This limits clinical applicability of these methods. To reduce the computation cost caused by 3D-CNN and improve the detection efficiency, Lu et al. [13] proposed a 2D CNN method, which is an integrated learning mechanism for CMB detection. Despite the low computational cost of 2D CNN, it suffers from the problem of spatial information loss in 2D analysis of 3D MRI images [14,15]. Specifically, such 2D CNN based methods are prone to be affected by the angle of view in 2D space and cannot exclude a large number of false positive samples. For example, CMBs always occur near the cerebral vessels. In the three-dimensional view, cerebral microbleeds are spherical while vessels are tubular in shape. When the vessels are locally observed on an MRI slice, their morphology is very similar to CMBs. As shown in Fig. 1, in the transverse plane, blood vessels appear to be indistinguishable from the CMBs from the perspective of size and shape [11,16]. Therefore, multi-perspective observation is necessary to eliminate those false positive samples.

On the other hand, medical imaging data is relatively difficult to be obtained due to patient privacy issues. Thus the lack of data is a common problem that existing deep learning methods face in object detection, segmentation and disease diagnosis research based on medical images [17,18]. Although there have been many research works related to CMB detection, there are still few publicly available datasets [16,19–21]. Meanwhile, the annotation of the CMB dataset usually requires the participation of several skilled clinicians and is a tedious and time-consuming work. Therefore, how to reduce the workload of data annotation and avoid over-fitting under a limited sample size is the key technical problem of deep learning model design.

Traditional deep learning methods focus on extracting visual information from images, but ignore the location information of the detected object in the images. In the existing 2D and 3D CNN methods which perform detection with local (2D and 3D) patches, only the appearance information of CMBs in local patches was considered, ignoring the position information of the patches in the whole brain. In fact, the position of a patch contains the probability information of the occurrence of CMBs. A large number of clinical studies have proved that CMBs have a certain distribution pattern in the brain [22,23], which is related to the occurrence and development of different diseases such as hypertensive angiopathy, cerebral infarction, and neurodegenerative diseases [24–26]. We statistics the distribution of the number of cerebral microbleeds in the SWI-CMB training set (16 patients) on each slice in the transverse, coronal, and sagittal planes, as shown in Fig. 2. It is not difficult to find that cerebral microbleeds are not evenly distributed in the brain and are more dense in some areas. Motivated by this domain knowledge, in this paper, we are aiming at introducing the position information of CMBs into the deep learning network to reduce the false positive results.

This paper aims to study an effective and efficient CMB detection method. Our novel model is called Knowledge-guided Body Plane Network (KBPNet), which can significantly reduce the number of false-positives. The efficiency of the proposed model mainly benefits from two key components. First, a 2.5D CNN model, which stands as a compromise between the 2D and 3D CNN methods, is proposed. Transverse, coronal, and sagittal CMB patches are combined and used as inputs for the 2.5D CNN detector. Indeed, this method does not only utilize 3D spatial information, but it also reduces the computational cost. Second, priori knowledge is fused into the model. The global CMB distribution is statistically estimated and the priori knowledge is used to guide our network.

In summary, the main contributions of this paper are as follows:

- First, we propose a novel two-step method for CMB detection, which only needs to train a 2D CNN network but can fulfill the two-step 2.5D body plane detection. The proposed 2.5D body-plane CMB detection network greatly reduces the computational complexity compared with 3D convolution while exploiting the spatial information of MRI images.
- Second, we develop a simple and reusable 2D backbone CNN. Its simplicity and ease of training relieve the problem of network overfitting under small data volume. Furthermore, our experiments have demonstrated that the proposed network can obtain a satisfactory detection only in the first step and the false positive results can be reduced significantly through using priori knowledge. This greatly improves the detection efficiency.
- Third, we fuse the priori knowledge of CMB vulnerable areas into the model. This priori knowledge can be regarded as a regular pattern that certain regions of the brain (e.g., lobes and deep brain regions) are more prone to cerebral microbleeds. In our method, the position information of the patches plays a guiding role in model reasoning to enhance its decision-making ability. At the same time, the use of priori knowledge makes our small backbone network model more robust, which is shown in that the model can face a small number of training samples, and can be shared and reused in heterogeneous image detection. Finally, our experiments demonstrate that the approach proposed in this study results in a significant reduction in the average number of false positives per patient.

The remainder of this paper is organized as follows: Section 2 reviews the related work of CMB detection, deep learning as well as domain knowledge. In Section 3 we describe the dataset and data preprocessing used in this study. In Section 4, we present the workflow of our method and give a detailed description of our model and its main modules. Section 5 presents the experimental results and comprehensive analysis. Section 6 concludes the whole paper and look into the future work.

2. Related work

The "gold standard" for CMB detection was presumably established at the 2009 meeting of the Microbleed Study Group [1]. Recent studies have shown that CMBs are closely associated with cerebrovascular disease and cognitive impairment. Therefore, accurate and timely detection of CMBs is helpful for clinicians to diagnose such malignancies.

The CMB detection methods can be roughly divided into three categories, namely: manual detection methods, semi-automatic detection methods, and fully automatic detection methods.

In manual detection methods, screening for CMBs is essentially performed by well-trained radiologists. However, this process is notorious for being time-consuming, labor-intensive, and especially prone to subjective errors (as different experts may come up with different and inconsistent judgments for the same clinical case).

For semi-automatic detection, traditional digital image processing or machine learning methods are typically used to find candidate CMB patches. Then, experienced clinicians manually review the candidate CMB patches in order to exclude false-positive detections. While the semi-automatic approach generally surpasses the purely manual one, it still cannot entirely eliminate the subjectivity errors associated with manual identification. Barnes et al. [27] took the lead in proposing a semi-automatic CMB detection method. In their work, hypointensity points were found in MRI images through a thresholding algorithm, and then a support vector machine (SVM) was trained to differentiate between real and false-positive CMB detections, with a sensitivity of 81.7%. Fazlollahi et al. [28] used a multi-scale Laplacian-Gaussian filter to detect candidate CMBs and their corresponding bounding boxes. Then, 3D features based on Radon and Hessian measures were extracted

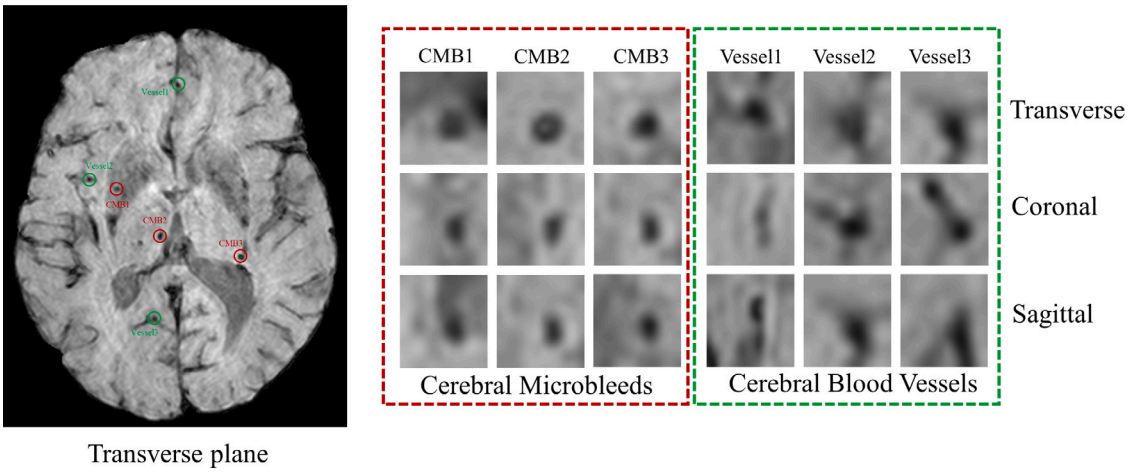

Fig. 1. True CMBs (in red circles) and false CMBs (in green circle) observed in a transverse plane. Herein the false CMBs are caused by cerebral blood vessels since they appear as hypointensity as CMB lesions. The CMBs are ellipsoidal in 3D space, so they can be observed as hypointensity lesions in the transverse, sagittal, and coronal plane. Whereas the cerebral blood vessels are tube-shaped structures which appear as hypointensity lesions in the transverse plane, but appear as lines in the coronal and sagittal planes.

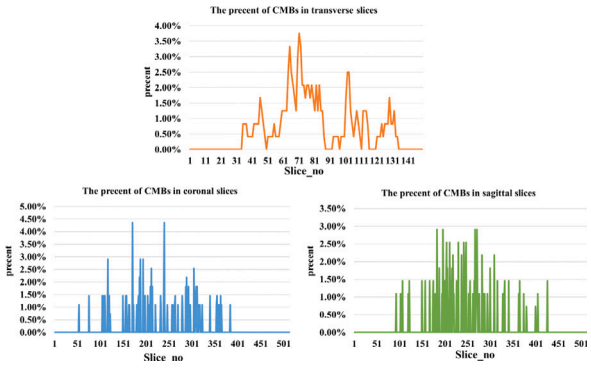

Fig. 2. Percentage curves of CMBs distribution in transverse, coronal and sagittal slices from 16 patients in SWI-CMB training dataset.

for each bounding box. These features were used to train a cascaded random forest, which achieved a sensitivity of 87% and an average false-positive count of 27.1.

In recent years, fully-automatic deep-learning-based CMB detection has become a research hotspot. Currently, automatic CMB detection methods can be broadly classified into three approaches: 2D CNN, 3D CNN or a mixture of 2D CNN and 3D CNN. Lu et al. [13] proposed a 2D CNN called FeatureNet, where the set of three classifiers was used for CMB detection with a sensitivity of 97.79%. Li et al. [29] proposed a 2D CNN with enhanced low-level features (called SSD-512) and achieved a sensitivity of 90%. Dou et al. [11] first proposed a two-stage CMB detection model based on 3D CNN. The first stage first used 3D FCN to obtain CMB candidate patches, and the second stage used 3D CNN for further evaluation to exclude false positive results. The sensitivity of this method was 93.2%, the accuracy was 44.71%, and the average number of false positives was 2.7. Liu et al. [30] proposed the use of SWI and high-pass filtered 3D phase images to eliminate the effect of calcification deposition. In addition, some researchers have proposed hybrid models based on 2D CNN and 3D CNN. For example, Al-Masni et al. [12] used a 2D CNN and 3D CNN cascade architecture to detect CMB. First, YOLO was used to select candidate CMB regions. Second, a cube centered on these candidate regions was used to train a 3D CNN detector with a sensitivity of 94.63% and an average false false-positive count of 1.42. In general, these deep-learning-based CMB detection methods have to face high calculation cost. Moreover, a large number of samples and labels required to train network are difficult to obtain in the medical field. This makes these methods difficult to apply in practical applications.

In some medical image processing work [14,15,31,32], 2.5D CNN is used as a compromise to balance the huge computational cost of 3D convolution and the insufficient access to spatial information of 2D convolution . For example, in order to incorporate valuable 3D information while preserving the required 2D input shape, Saint-Esteven et al. [14] used 2.5D CNN for HPV prediction, and Zheng et al. [15] used 2.5D CNN to force the model to learn features about inter-slice information, encouraging the communication between slices.

Nowadays, the use of domain knowledge in machine learning is a hot topic [33–35]. Li et al. [36] exploited both field measurements and satellite observations to provide a general form of priori knowledge and apply it to remote sensing inversion. Liang et al. [37] integrated the anatomical information of the white matter in the brain as priori feature into the UNet network to achieve more accurate segmentation of the white matter. What is more, Momeni et al. [38] generated a synthetic dataset by using the statistical information on the location and size of CMBs in real dataset as a priori knowledge to synthesize CMB lesions and put them into high-risk regions. Their experimental results show that the trained model using the synthetic dataset together with the real dataset is better than using the real dataset alone. This suggests the effectiveness of the distribution pattern of cerebral microbleeds.

In this study, we use a 2.5D body plane detection framework to compensate the spatial information loss of 2D CNNs and avoid the redundant calculation of 3D CNNs. Meanwhile, to lighten the whole network and address the lack of MRI data, we employ a simple 2D CNN network. The main difference between our two-step method and other existing methods lies in two aspects. First, we use only one trained 2D CNN network to fulfill the two-step 2.5D body-plane detection and the results of the two steps are combined to make a final decision. In contrast, the existing similar methods [11,30,39–41] use two different CNN networks in two stages, which requires a certain amount of training data. Second, the existing methods ignores the position clue which is important for an experienced clinical neurologists to read MRI slices, whereas we use the CMB statistics distribution as priori knowledge to guide the model learning and inferring. This enhances the discrimination ability of the model.

3. Dataset and data preprocessing

In this section, we first describe the employed data in our main experiments and introduce four data preprocessing steps.

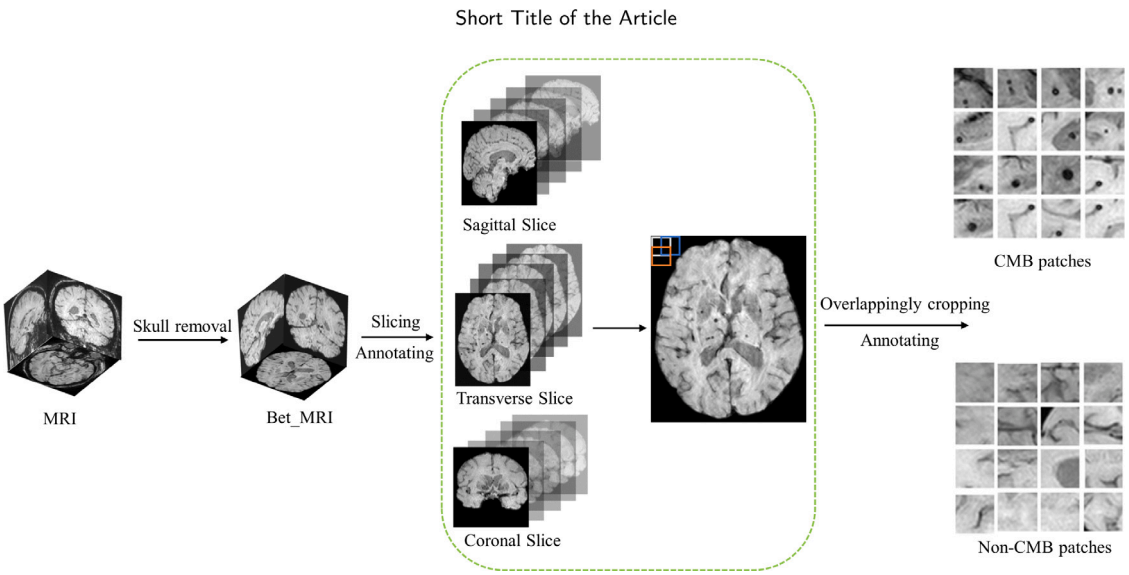

Fig. 3. MRI data preprocessing before CMB detection. For each MRI volume, the skull region is firstly removed by the Bet tool. Then, the volume is converted into slices and each slice is labeled. The slices are thus converted into annotated patches. Finally, CMB and non-CMB patches are obtained.

3.1. Dataset description

Because SWI is very sensitive to blood deposition, this imaging modality has been widely used in hemorrhagic lesion examinations. In this work, we mainly used the SWI-CMB dataset proposed by Dou et al. [11] in 2016 to validate the model. At present, this dataset provides MRI brain volumes for downloading.

SWI-CMB acquired from 20 patients with CMBs using a 3-Tesla MRI machine (Philips Medical System). Each of these MRI volumes has a size of 512 × 512 × 150 mm, an in-plane resolution of 0.45 × 0.45 mm, a slice thickness of 2 mm, a slice spacing of 1 mm, and a field of view of 230 × 230 mm^2. The overall CMB count is 74 where the per-patient CMB count ranges from 1 to 13, ground-truth is the 3D center-of-mass coordinate of each CMB. In our analysis and evaluation experiments, we used the data of 16 patients for training and the data of 4 patients for testing.

3.2. Data preprocessing

Patch-wise retrieval is applicable and often is applied to medical image analysis. On one hand, it can address the problem of positive sample insufficiency in available clinical data. On the other hand, it can reduce the network parameters. In this study, we employed a 2D-patch based detection approach. Therefore, we performed a series of data preprocessing on the original dataset to construct a patch-level dataset. Firstly, we transferred the MRI images into slices in coronal, sagittal, and transverse planes individually. We labeled the adjacent slices in the transverse plane according to the ground-truth centroid coordinates to obtain the CMB coordinate position of each transverse slice. Then we converted these slices to patches and labeled the patches. Finally, we construct a dataset consisting of about 1.7 million patches images and their annotations. Fig. 3 illustrates the involved four data preprocessing steps.

3.2.1. Skull removal

To reduce the influence of the calvarial bone region on the CMB detection results, we first removed the skull area by performing the bet operation on each raw MRI volume using the Bet tool [42] of the FMRIB Software Library (FSL).

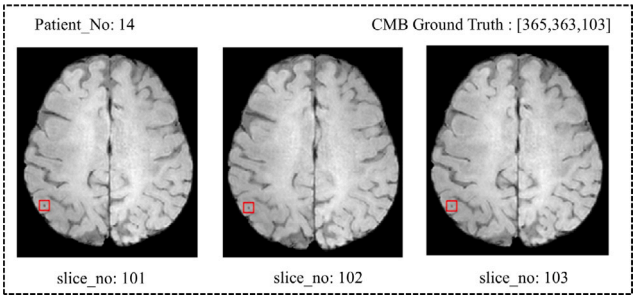

Fig. 4. Cerebral microbleed (groundtruth coordinate is [365, 363, 103]) visualized on adjacent slices.

3.2.2. MRI slicing and annotating

The next step is to slice the 3D MRI volume of each patient. Taking the transverse, coronal, and sagittal directions as axes, we obtained 150 slices in the transverse direction, and 512 slices in each of the coronal plane and sagittal directions. For each CMB lesion, the SWI-CMB dataset includes the ground-truth labeled by its 3D centroid coordinates. Since the real CMB lesion has an ellipsoid shape with a volume, it can be observed on multiple adjacent slices. For example, as shown in Fig. 4, the 14th patient has a hypointensity lesion (within the red box) whose ground-truth centroid coordinates are [365, 363, 103]. The coronal, sagittal, and transverse plane coordinates are recorded as X, Y, and Z respectively. If the adjacent slices containing CMB are not labeled, they will be marked as negative samples when cropping the patches, which will interfere with the inference of the model. What is more, we want to make full use of the existing CMB coordinates to obtain more patches containing CMB. Therefore, we manually labeled the adjacent visible slices of each CMB in the SWI-CMB dataset according to the given centroid coordinates, keeping the X-axis and Y-axis coordinates unchanged, capturing five slices before and after the Z-axis, and then identify its presence at the same position of these slices. Finally, slice annotation data is obtained for all CMBs.

3.2.3. Slice cropping and annotating

The SWI-CMB dataset contains a variable number of CMBs for each patient where the size and extent of each CMB is very small. Indeed, the numbers of the positive samples at the patient level or the slice-level

are quite insufficient for model training. To overcome this problem, we collect samples at the patch-level where each patch has a fixed size of 48 × 48 mm, and the location of each patch is specified by the coordinates (P_x, P_y) of its upper-left corner. Given a CMB coordinate (C_x, C_y), we determine whether a patch (P_x, P_y) is a positive sample according to:

$$P_{\text{label}}\ (P_x, P_y) = \begin{cases} 1 & 0 \le D_x, D_y \le 48 \\ 0 & \text{Otherwise} \end{cases} \quad (1)$$

where $D_x = C_x - P_x$ and $D_y = C_y - P_y$. To reduce the influence of the CMBs located at patch boundaries, we extract overlapping patches with an overlap stride of 1/2 of the patch size (i.e., 24 mm). It should be noted that the ratio of the number of slices with no CMBs to the number of slices containing CMBs is indeed very large, originally nearly 1600000:1200 in the dataset used. To address the problem of class imbalance, we followed a random downsampling strategy [43–45]. In the random sampling process, due to black patches are considered less informative, we first performed a black patch removal operation: A binary threshold is applied to each patch and the percentage of black pixels (i.e.pixel value is 0) is calculated. If the black pixel percentage of a patch exceeds 95%, the patch is discarded. Subsequently, we randomly selected negative samples from the remaining ones and made the ratio of negative to positive samples approximately 1:1.

3.2.4. Data augmentation

Although the aforementioned data preprocessing step expanded the 74 raw CMBs to 724 positive patches with CMBs, this number of samples was still insufficient for deep model training. Therefore, we further expanded the training sample size through data augmentation. In particular, the positive patches containing CMBs were rotated clockwise by 90°, 180°, and 270° and were also translated horizontally and vertically. No other operations or rotation angles were considered to avoid the possibility of moving the CMBs (whose positions are not known with high uncertainty) outside of the image boundaries after these operations (the samples would not be positively labeled in this case). So, through the above mentioned five augmentation operations, the number of positive samples was multiplied six times (i.e., 4344 positive samples with CMBs became available for training).

4. Knowledge-guided 2.5D CNN

This paper aims to develop a lightweight and applicable network for real-world CMB detection task. In our network, we integrate CMB risk knowledge and adopt a 2.5D body plane detection strategy. In this section, we present the detailed description of our Knowledge-guided 2.5D CNN model.

4.1. Overall network framework

As mentioned above, our KBPNet is a one-step training and two-step detection framework. In our method, a single-branch network is trained using single-plane data in one-step training and then the trained model is reused in different steps of the two-step detection. Fig. 5 shows the overall KBPNet architecture and the two-step detection workflow. First, a simple 2D CNN (Its implementation details is given in Section 5.2) is trained based on image patches of the transverse plane from the training dataset. Then the well-trained network is applied to CMB detection. The detection workflow includes two steps: preliminary screening (First Step in Fig. 4(a)) based on the transverse plane and fine screening (Second Step in Fig. 4(b)) based on 2.5D body plane.

Preliminary screening

In the preliminary screening phase, we identify all candidate cerebral microbleed patches in transverse plane by means of a classifier combined with a priori knowledge of cerebral microbleed distribution. In this step, patch-level samples are firstly fed to our 2D convolutional network, which simply contains two convolution layers. The network configuration will be given in Section 5.2. Besides image patch information, we also exploit the position information of patches. Specifically, the CMB probability of an image patch is calculated by a binary classifier according to the image features obtained by the backbone network. At the same time, the CMB risk value of the patch is obtained by retrieving in a priori knowledge base according to its location. Finally, the CMB probability and risk values are weighted to determine candidate CMB patches, as shown in Fig. 4(a).

Fine screening

There may be false positives among the candidate patches returned by the preliminary screening step. Therefore, the candidate CMB patches should be further examined to remove false-positive samples. To make the network lightweight and improve the accuracy of our method, we employ a 2.5D strategy. To generate the 2.5D body plane, we first use a blob detection algorithm(BDA) [46] to find the CMB locations in each candidate CMB patch. Then, the CMB locations are mapped to the original 3D coordinates, and each candidate CMB is taken as the center of a cube where the coronal and sagittal patches intersect. Thus, for each candidate CMB patch, coronal, sagittal, and transverse plane information is obtained and sent through our model and fused with weighted averaging for further classification, as shown in Fig. 4(b).

4.2. Priori knowledge construction based on ground-truth

Clinical studies have shown that CMBs are not evenly distributed throughout the whole brain, but usually occur in the brain lobes and the deep brain regions (i.e., the basal ganglia, the thalamus, the deep white matter, and the infratentorial region) [9]. Therefore, we conjecture that the cerebral microbleed distribution in the available data can be used as priori knowledge to guide the model to judge CMBs more accurately.

Suppose we have collected CMB MRI data, $D^{\mathcal{K}} = \{M_i \mid i = 1,\ldots, K\}$, from K patients. We can learn CMB knowledge $\mathcal{K}$ based on SWI-CMB dataset, i.e., where cerebral microbleeds are more likely to occur in the brain. To train a model, we can utilize the ground-truth CMB labels in the training data. Let $D = \{T, V\}$, where D is the dataset, which is divided into the training subset T and the testing subset V, and T and V is mutually exclusive. Herein, $D^{\mathcal{K}} = T$.

We use a Gaussian kernel function to generate a heatmap as priori knowledge for CMB detection. The priori knowledge base involves N heatmaps, representing CMB risk values corresponding to different spatial locations, where N denotes the slice number in transverse plane (N = 150 in SWI-CMB). The priori knowledge construction based on the ground-truth is described as follows:

We collect the CMBs in each transverse slice from T and generate Gaussian heatmaps of the CMB risk. For each slice, these CMB heatmaps are summed over K patients in training samples and then added to the priori knowledge base $\mathcal{K}$.

Let $\mathcal{K} = \{H_i;\ i=1,\ldots, N\}$, where H_i denotes the ith heatmap corresponding to the ith transverse slice. The Gaussian heatmaps are CMBs on each slice are summed.

$$\boldsymbol{H}_i = \sum_{i=1}^{m} h_i^j \quad (2)$$

where h_i^j is the heatmap corresponding to the jth CMB from the ith transverse slice, m represent the CMB number on each slice and

$$h_i^j = \begin{cases} \exp\left(-\frac{\left(x-x_i^j\right)^2+\left(y-y_i^j\right)^2}{2\sigma^2}\right), (x,y) \in \Omega \\ 0 \end{cases} \quad (3)$$

where $(x_i^j,\ y_i^j)$ is the coordinate of the jth CMB in the ith transverse slice, and $(x,\ y)$ is the neighborhood of $(x_i^j,\ y_i^j)$ with radius σ which is setted 9 in SWI-CMB.

By the above mentioned construction method, we obtained the priori knowledge of cerebral microbleeds, representing the probability

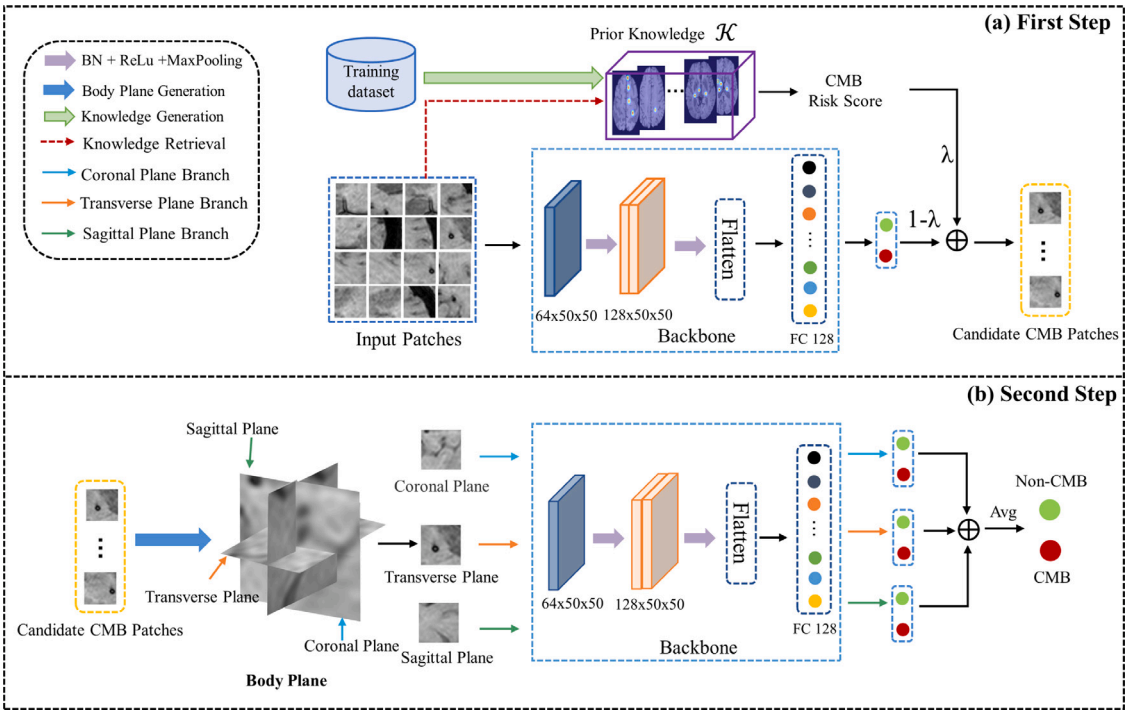

Fig. 5. Overall KBPNet architecture and workflow. (a) First Step: Perform preliminary screening. (b) Second Step: Perform fine screening. To reduce redundant calculations, the transverse plane reuse the classification results of the first step.

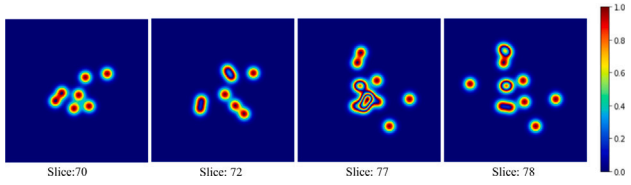

Fig. 6. Priori knowledge of cerebral microbleeds in SWI-CMB training set. The colored bright spots represent the visualization of cerebral microbleeds after Gaussian kernel functions, and the overlap in the bright spots indicates a higher incidence in this region.

of having CMB in each part of the brain, the brighter the region represents the higher risk value of having cerebral microbleed lesions in that region, and the visualization results of the priori knowledge are shown in Fig. 6.

4.3. CMB risk score

When evaluating the candidate CMB patches in the first step, we add priori knowledge $\mathcal{K}$ to boost the classification performance in the preliminary screening step. This method effectively exploits the spatial information of the whole brain and the CMB distribution in the evaluation of the local CMB patches. For each transverse patch $\boldsymbol{p}_t$, the CMB risk score s_t is defined as:

$$s_t = \frac{e^{-\max\left(H_{x,y}|(x,y)\in \boldsymbol{p}_t\right)}}{1+e^{-\max\left(H_{x,y}|(x,y)\in \boldsymbol{p}_t\right)}} \tag{4}$$

where $H_{x,y}$ represents the heat value of the position (x, y) in the transverse patch $\boldsymbol{p}_t$. Denote the final CMB probability value of transverse patch in the first step as $\hat{g}'_t$.

$$\hat{g}'_t = (1-\lambda)\Phi\left(\boldsymbol{p}_t\right) + \lambda s_t \tag{5}$$

where $\Phi\left(\boldsymbol{p}_t\right)$ represents the CMB probability obtained through CNN in the patch channel, and s_t represents the a priori CMB risk score of the transverse patch $\boldsymbol{p}_t$, and λ is a hyperparameter.

4.4. Body plane module: 2.5D CNN

The module is shown in the Second Step in Fig. 4(b), where we combine the transverse, coronal, and sagittal patches of each candidate cerebral microbleed to exclude false positive results. In the training phase, we use the transverse patches combined with priori knowledge to train the backbone network. In the testing phase, the trained backbone network first is used with transverse patches for preliminarily screening to find candidate CMBs, and then in the second step is reused with the corresponding coronal and sagittal patches. Finally, the evaluation results of three planes are combined for final classification decision.

To reduce calculation and reuse the classification results in the first step, we design a more cost-effective body-plane-based CMB detection scheme, detailed as follows:

Unique CMB Absolute Coordinate Determination

The BDA [46] is used to locate suspicious CMB targets in the candidate CMB patches, and then the patches containing the same CMB are merged. Suppose the set of candidate CMB patches obtained in the first step is $P = \{\boldsymbol{p}_{t_i}, t_i = 1, \ldots, M\}$. Denote each transverse patch as $\boldsymbol{p}_t = ((P_x, P_y), I, J)$, (P_x, P_y) is the upper left corner coordinate of $\boldsymbol{p}_t$, I is the slice index and J is the patient index.

Given a suspicious CMB target q detected by BDA, and its relative coordinate in the patch $\boldsymbol{p}_t$ which contains q is (C_x, C_y). As shown in Fig. 7(a), the absolute coordinate of q is $(P_x + C_x, P_y + C_y)$. As we use overlap method to partition the images, the same CMB may be contained in different patches, as shown in Fig. 7(b). We merge the patches which contain the same CMB target b into a set $Q_b = \{q_i, i = 1, \ldots, n_b\}$, and $\exists \quad C_x^{q_i} + P_x^{q_i} = C_x^{q_j} + P_x^{q_j} \quad \& \quad C_y^{q_i} + P_y^{q_i} = C_y^{q_j} + P_y^{q_i} \quad \& \quad I^{q_i} = I^{q_j} \quad \& \quad J^{q_i} = J^{q_j}, i \neq j.$

As a result, we obtain all the suspected CMB targets and record their absolute coordinates in a list.

Body Plane Generation

For each suspected CMB target in the list, we centered on it and cut out patches of size 48 × 48 mm in the coronal and sagittal planes, respectively, denoted as $\boldsymbol{p}_c$, $\boldsymbol{p}_s$. Subsequently, these coronal and sagittal patches are fed into the backbone network as input.

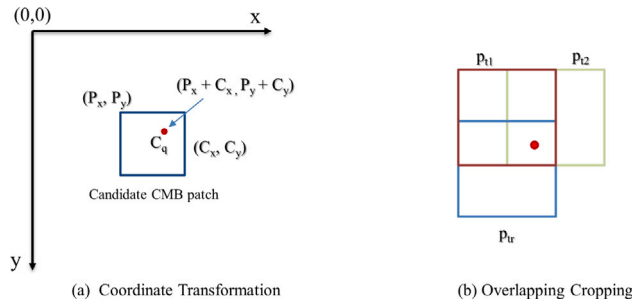

Fig. 7. CMB absolute coordinate determination.

Weighted Summation

Firstly, to reduce redundant computing, we reused the transverse classification results in the first detection step. Additionally, the classification results of the patches which contains the same suspected CMB target are averaged as the evaluation value in transverse plane of the CMB target. Namely, given a suspected CMB target b and its corresponding transverse patch set Q_b, then

$$\hat{g}_t = \frac{1}{n_b}\sum_{i=1}^{n_b}\hat{g}'_{t_i} \tag{6}$$

where n_b denote the patch number in Q_b, $\hat{g}'_{t_i}$ is the classification results in the first step of the patch q_i in Q_b. Then, for each suspected CMB target b, its final CMB probability value $\hat{g}$ in the second step is the average sum of the three classification results,

$$\begin{aligned}\hat{g} &= \frac{1}{3}\left(\hat{g}_s + \hat{g}_t + \hat{g}_c\right)\\ &= \frac{1}{3}\left(\boldsymbol{\Phi}\left(\boldsymbol{p}_s\right) + \hat{g}_t + \boldsymbol{\Phi}\left(\boldsymbol{p}_c\right)\right)\end{aligned} \tag{7}$$

Where $\hat{g}_s$, $\hat{g}_t$ and $\hat{g}_c$ denote the classification results based on the patches from the sagittal, transverse, and coronal planes, respectively.

5. Experimental results

In this section, we first introduce the details of the experiment setup, network configuration, loss function and evaluation metrics. Then, we present the model validation results and give comprehensive model analysis and discussions. Finally, the drawbacks of the model are given.

5.1. Experimental setup

The model was implemented within the PyTorch framework. The operating system was Ubuntu 18.04 and the model training and testing were performed on an NVIDIA 2080ti GPU, with an Adam optimizer, a fixed learning rate of 0.0001, a training iteration count of 50, and a batch size of 64. The dataset were divided into training and testing subsets in the ratio of 8:2. To avoid sampling bias [20,47,48], we conducted the experiments with a 5-fold cross-validation scheme.

5.2. Network configuration

The components and parameters of the network architecture for the CMB detection model is shown in Table 1.

5.3. Loss function and evaluation metrics

We used a weighted sum of the cross-entropy loss

$$L_1 = -\left[l_i \cdot \log\left(p_i\right) + \left(1 - l_i\right) \cdot \log\left(1 - p_i\right)\right] \tag{8}$$

and the binary cross-entropy logit loss

$$L_2 = -w_i\left[l_i \cdot \log \Sigma\left(p_i\right) + \left(1 - l_i\right) \cdot \log\left(1 - \Sigma\left(p_i\right)\right)\right] \tag{9}$$

Table 1
Framework in detail.

Layer	Kernel size	Stride	Padding	Output size	Feature volumes
Input	–	–	–	48 × 48	1
Conv2d-1	3 × 3	1 × 1	2 × 2	50 × 50	64
BN-2	–	–	–	50 × 50	64
ReLU-3	–	–	–	50 × 50	64
MaxPool2d-4	2	1	0	49 × 49	64
Conv2d-5	3 × 3	1 × 1	2 × 2	51 × 51	128
BN-6	–	–	–	51 × 51	128
ReLU-7	–	–	–	51 × 51	128
MaxPool2d-8	2	1	0	50 × 50	128
Flatten-9	–	–	–	1 × 1 × 1	32000
Linear-10	–	–	–	1 × 1 × 1	128
ReLU-11	–	–	–	1 × 1 × 1	128
Dropout-12	–	–	–	1 × 1 × 1	128
Linear-13	–	–	–	1 × 1 × 1	2
Softmax-14	–	–	–	1 × 1 × 1	2

as the overall loss function

$$Loss = \eta L_1 + \mu L_2 \tag{10}$$

where η, μ represents weighted values of final loss function, and $\Sigma(.)$ denotes the sigmoid function, p_i denotes the predicted CMB probability of the ith sample while l_i denotes the corresponding ground-truth label. The second loss term L_2 was used to penalize CMB misclassification with a penalty weight w_i of 1.5.

We employed three commonly used performance indicators [29,49,50] to quantitatively evaluate the performance of the proposed CMB detection method: the sensitivity, precision, and the average false-positive number (FPavg) per patient. These indicators can be defined as follows:

$$Sensitivity = \frac{TP}{TP + FN} \tag{11}$$

$$Precision = \frac{TP}{TP + FP} \tag{12}$$

$$FP_{avg} = \frac{FP}{N} \tag{13}$$

where TP, FP, TN, and FN denote the true-positive, false-positive, true-negative, and false-negative counts, respectively, while N denotes the total number of patients.

5.4. Main results

Comparison experimental results are reported in Table 2. We reproduced the networks in [11,13,52,53], and conducted the comparison experiments on the SWI-CMB dataset. The results of [12,39,50,51] are directly from the published papers, where the authors used their private datasets. The network of Dadar et al.'s [52] is a fine-tuned ResNet50 pre-trained on the ImageNet dataset, and Lee et al.'s [53] is a fine-tuned EfficientDet D3 pre-trained on the COCO dataset. It can be seen that these pre-trained models using deep architectures lead to high computational costs. On the whole, our proposed method outperforms all these existing methods that use 2D CNN and 3D CNN networks in all performance metrics with less computational complexity. Our proposed model balances the problem of complex computational volume of 3D convolution while exploiting the spatial information of MRI.

The visualization results of the detection of cerebral microbleeds are shown in Fig. 8. Where red rectangles represent true cerebral microbleeds, white rectangles represent false positive results caused by blood vessels, and green rectangles represent false positive results in low risk regions. In Fig. 8, from left to right, the results of cerebral microbleeds detection without any module added, the results with the a priori knowledge module added, the results with the body module added, and the results with both modules added, respectively. In summary, false-positive results in regions with low risk of cerebral microbleeds can

Table 2
Comparison results of evaluation indicators.

Reference	Method	Layers	Flops	Sensitivity	Precision	FPavg
Chen et al. [50]	3D CNN	–	–	89.10%	–	6.4
Ghafryal et al. [51]	2D CNN	–	–	90.90%	–	4.1
Myung et al. [39]	2D CNN	22	4.06G	66.90%	79.75%	2.15
Al-masni et al. [12]	2D CNN + 3D CNN	11	2869.14M	94.32%	61.94%	**1.42**
Lu et al. [13]	2D CNN	15	172.20M	95.54%	88.37%	5.6
Dadar et al. [52]	2D CNN	50	3.86G	97.37%	83.80%	7.69
Lee et al. [53]	2D CNN	33	2.40G	92.61%	86.74%	3.86
Dou et al. [11]	3D CNN	12	1.12G	93.16%	44.71%	2.74
KBPNet(ours)	**2.5D CNN**	**15**	**706.95M**	**98.24%**	**94.10%**	**1.72**

Table 3
The running time of the model.

Model phase	Target	Time
First Stage	Obtain candidate CMB patches.	10.9 ms
Blob Detection	Located suspected cerebral microbleed.	0.056 ms
Crop Patches	Cut out patches in the coronal and sagittal planes with the suspected cerebral microbleed as the center.	2.63 ms
Second Stage	Exclusion of false positive results caused by cerebral vessels.	26.7 ms

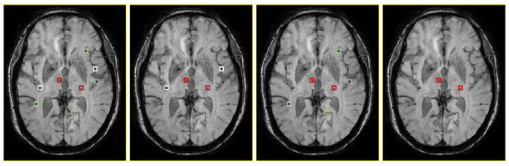

Fig. 8. Examples of CMB detection results by our method in SWI-CMB dataset(viewed in axial planes). Red rectangle denotes the real cerebral microbleeds and green rectangle denotes the removed false positive candidate by priori knowledge module in the first stage, white rectangle denotes the removed false positive candidate by body plane module in the second stage.

Table 4
Comparison results of different weighted values of the loss function.

η	μ	Sensitivity	Precision	FPavg
0.1	0.9	78.79%	96.30%	**0.50**
0.2	0.8	72.73%	96.00%	0.50
0.3	0.7	76.46%	95.89%	0.88
0.4	0.6	74.64%	95.56%	0.50
0.5	0.5	80.30%	96.36%	1.82
0.6	**0.4**	**96.97%**	**92.75%**	2.06
0.7	0.3	95.45%	90.00%	3.12
0.8	0.2	96.58%	87.67%	2.25
0.9	0.1	90.91%	88.24%	4.12

be excluded after the first stage, and false-positive results caused by cerebral vessels can be excluded after the second stage.

The running time of the model proposed in this paper mainly includes the preliminary screening in the first stage, the blob detection and cropping patches in the second stage, and the fine screening in the second stage. The time consumption is reported as shown in Table 3.

The main focus of our approach proposed in this study is to optimize the efficiency of the model detection process. However, the steps of data preprocessing still follow the traditional approach, including skull removal, slicing, annotation of slices, slices to patches, annotation of patches, data augmentation. These steps require additional time to complete.

5.5. Model analysis and discussion

5.5.1. Analysis of loss function

Since the cerebral microbleed detection task needs to reduce the underdiagnosis as much as possible. In other words, partial false-positive results can be tolerated while ensuring that true cerebral microbleeds are detected as much as possible. As for how to reduce the false-positive results, it is the challenge of this study. Therefore, we introduced the BCEWithLogitsLoss function to add a penalty for the case of missed diagnosis.

We explore the effect of different weighted values on the loss function, we present the experimental results in Table 4. According to the results, we set η=0.6 and $\mu = 0.4$ in our experiments.

5.5.2. Influences of λ

To verify whether the hyper-parameter λ of prior knowledge varies with the size of the dataset. We performed the validation on the SWI-CMB as well as on the PublicDataShare_2020 dataset [38], which is basically described as follows:

PublicDataShare_2020 acquired 58 patients with CMBs from 3.0T Siemens TRIM TRIO scanner, where SWI were reconstructed online using the scanner system (software VB17). Each of these MRI volumes has a size of 176 × 256 × 80 mm, 0.93 mm × 0.93 mm in-plane resolution and 1.75 mm slice thickness. The overall CMB count is 146, ground-truth is the 3D center-of-mass coordinate of each CMB. We used the data of 45 patients for training and the data of 13 patients for testing.

In our experiments, the hyper-parameter λ is empirically set 0.1 on the SWI-CMB [11] according to the results in Fig. 9 (a). More experiments on the PublicDataShare_2020 dataset demonstrate that λ = 0.1 is also an optimal setting, as shown in Fig. 9(b). Therefore, its setting may change little with the changes of the sample size and even the dataset. We think The priori knowledge base provides the risk value of CMB occurrence in the neighborhood region centered on a real CMB. We suppose that the priori knowledge base can be regarded as a soft label, which can enhance the confidence of cerebral microbleed detection results in high-risk regions and weaken that in low-risk regions. λ determines the impact intensity of this item in the decision.

5.5.3. Influences of σ

We use Gaussian kernel functions to generate a priori knowledge heatmaps. The ground truth coordinates of the CMBs were used as the center and σ was the fixed Gaussian kernel standard deviation to generate priori knowledge as the probability of CMB risk for this CMB and its neighbors. However, as mentioned in the related literature [54], it is suggested that the fixed Gaussian kernel standard deviation ignores human scale differences in human pose estimation, which significantly affects the accuracy of the estimation. Therefore, it is reasonable to generate heatmaps using different kernel standard deviations that are adaptive to different scales. There is a scale difference between the two datasets used by this paper. Specifically, SWI-CMB has a dimension

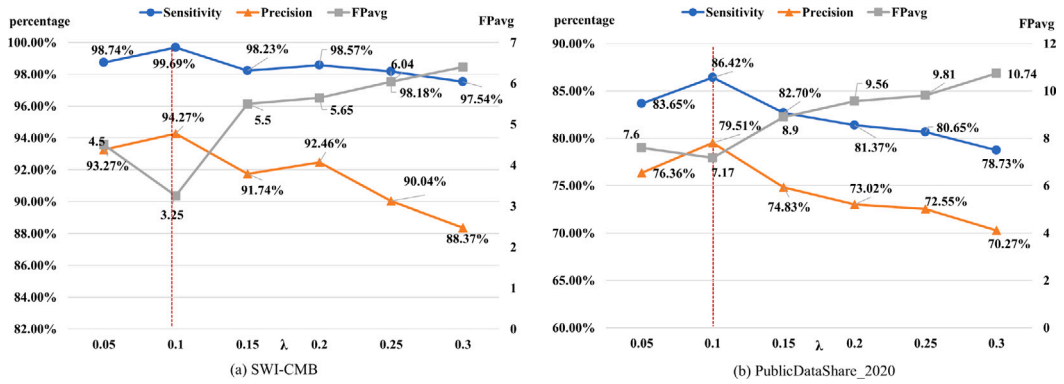

Fig. 9. λ hyperparameter determination by sensitivity, precision and FPavg in SWI-CMB and PublicDataShare_2020.

Table 5
Ablation experiment results.

Dataset	Knowledge	2.5D Plane	SWI-CMB			PublicDataShare_2020		
Method			Sensitivity	Precision	FPavg	Sensitivity	Precision	FPavg
KBPNet	✗	✗	95.54%	88.37%	5.60	74.13%	69.74%	13.19
KBPNet	✔	✗	97.57%	92.46%	3.00	86.42%	79.51%	7.17
KBPNet	✗	✔	96.23%	91.74%	4.50	75.36%	70.15%	12.72
KBPNet	✔	✔	**98.24%**	**94.10%**	**1.72**	**87.54%**	**81.63%**	**6.54**

of 512 × 512 in the transverse plane while 176 × 256 for PublicDataShare_2020. The scale difference is more than two times, and thus the standard deviation of the Gaussian kernel needs to be adjusted.

Cumulative dynamic update of the knowledge base based on a larger cerebral microbleeds dataset on the same MRI device, enabling the acquisition of a priori knowledge become more and more able to reflect the distribution of CMBs.

5.5.4. Ablation study

The proposed KBPNet model achieves improvements mainly via the priori knowledge and body plane modules. To validate the effectiveness of each module, we conducted ablation experiments and reported the results in Table 5. The addition of the priori knowledge module to the backbone structure resulted in improved sensitivity and precision for these datasets and a decrease in the average number of false positives, which proved the effectiveness of the module. In addition, all metrics were improved after adding the body plane module to the backbone structure, which proved the effectiveness of the module. Finally, all metrics improved after the introduction of both modules. This proves the effectiveness of our proposed method.

5.5.5. Shortcoming

- Some hyperparameters in the model are not set intelligently enough, such as the weighted hyperparameter λ of the priori knowledge base and the μ and η of the loss function, which need to be set manually for multiple control experiments to select a better solution. An automated fine-tuning scheme may be considered to learn the hyperparameters.
- Due to the differences in image size of different datasets, our model has a decreased experimental performance at lower image resolutions, such as PublicDataShare_2020.

6. Conclusions and outlooks

We have proposed a simple and effective CNN model for cerebral microbleeds detection. Existing CMB detection methods based on 3D or 2D patches ignore different risk of CMB in different areas of the whole brain. In this study, we generate CMB risk heatmaps to construct a priori knowledge base, by which we can retrieve the risk score of CMB at each position in the whole brain and guide the model to determine candidate cerebral microbleeds patches. To solve the problems of redundant computation in 3D CNN and loss of spatial information in 2D CNN, a 2.5D CNN model is proposed in this paper. Coronal, sagittal and transverse information of candidate CMB patches are used simultaneously to obtain spatial feature representation to morphologically exclude false positive results. Our approach is simple to train compared to other two-stage models since only one model needs to be trained. Experimental results show that our proposed model maintains better sensitivity, accuracy and lower average number of false positives while reducing the computational effort.

In future work, larger cerebral microbleed datasets is necessary to cumulatively update the priori knowledge base so that the acquired priori knowledge becomes increasingly reflective of the CMB distribution. Means of medical registration is also needed to obtain anatomical structure of the human brain, which can be used as priori knowledge together with the CMB statistical information to better guide model learning. Additionally, semi-supervised or self-supervised methods can be introduced to increase the automation of data annotations. Finally, more theoretical and methodological research on the combination of domain knowledge and in-deep learning is also the focus of our work.

CRediT authorship contribution statement

Zhongding Fang: Methodology, Formal analysis, Data curation, Writing – original draft, Visualization. **Rong Zhang:** Conceptualization, Investigation, Writing – review & editing, Funding acquisition, Supervision. **Lijun Guo:** Conceptualization, Investigation, Writing – review & editing. **Tianxiang Xia:** Resources, Investigation, Validation. **Yingqing Zeng:** Resources, Investigation, Formal analysis. **Xiping Wu:** Methodology, Software, Validation.

Declaration of competing interest

The authors declare that they have no known competing financial interests or personal relationships that could have appeared to influence the work reported in this paper.

Data availability

Data will be made available on request.

Acknowledgments

This research work is partly supported by the Zhejiang Provincial Public Welfare Technology Research Project (No. LGF21F020008), Ningbo Municipal Public Welfare Technology Research Project (No. 2022S134), the Open Project Program of the State Key Lab of CAD & CG (No. A2119), Zhejiang University.

References

[1] M. Viswanathan, R. Salman, M. Steven Warach, J. Lenore, Cerebral microbleeds: a field guide to their detection and interpretation, Lancet Neurol. 8 (2) (2009) 165–174.
[2] M. Fisher, S. French, P. Ji, R.C. Kim, Cerebral microbleeds in the elderly: a pathological analysis, Stroke 41 (12) (2010) 2782–2785.
[3] M.A. Ferlin, M. Grochowski, A. Kwasigroch, A. Mikołajczyk, E. Szurowska, M. Grzywińska, A. Sabisz, A comprehensive analysis of deep neural-based cerebral microbleeds detection system, Electronics 10 (18) (2021) 2208.
[4] H.-H. Tsai, M. Pasi, L.-K. Tsai, Y.-F. Chen, Y.-W. Chen, S.-C. Tang, M.E. Gurol, R.-F. Yen, J.-S. Jeng, Superficial cerebellar microbleeds and cerebral amyloid angiopathy: a magnetic resonance imaging/positron emission tomography study, Stroke 51 (1) (2020) 202–208.
[5] S. Shams, T. Granberg, J. Martola, X. Li, M. Shams, S.-M. Fereshtehnejad, L. Cavallin, P. Aspelin, M. Kristoffersen-Wiberg, L.-O. Wahlund, Cerebrospinal fluid profiles with increasing number of cerebral microbleeds in a continuum of cognitive impairment, J. Cereb. Blood Flow Metab. 36 (3) (2016) 621–628.
[6] H.-H. Tsai, L.-K. Tsai, Y.-L. Lo, C.-H. Lin, Amyloid related cerebral microbleed and plasma Aβ40 are associated with cognitive decline in Parkinson's disease, Sci. Rep. 11 (1) (2021) 1–9.
[7] S. Nannoni, L. Ohlmeier, R.B. Brown, R.G. Morris, A.D. MacKinnon, H.S. Markus, DNA Lacunar 2 investigators, Cognitive impact of cerebral microbleeds in patients with symptomatic small vessel disease, Int. J. Stroke 17 (4) (2022) 415–424.
[8] A. Charidimou, D.J. Werring, Cerebral microbleeds: detection, mechanisms and clinical challenges, Future Neurol. 6 (5) (2011) 587–611.
[9] J.M. Wardlaw, E.E. Smith, G.J. Biessels, C. Cordonnier, F. Fazekas, R. Frayne, R.I. Lindley, J. T O'Brien, F. Barkhof, O.R. Benavente, et al., Neuroimaging standards for research into small vessel disease and its contribution to ageing and neurodegeneration, Lancet Neurol. 12 (8) (2013) 822–838.
[10] G. Sparacia, F. Agnello, G. La Tona, A. Iaia, F. Midiri, B. Sparacia, Assessment of cerebral microbleeds by susceptibility-weighted imaging in Alzheimer's disease patients: a neuroimaging biomarker of the disease, Neuroradiol. J. 30 (4) (2017) 330–335.
[11] Q. Dou, H. Chen, L. Yu, L. Zhao, J. Qin, D. Wang, V.C. Mok, L. Shi, P.-A. Heng, Automatic detection of cerebral microbleeds from MR images via 3D convolutional neural networks, IEEE Trans. Med. Imaging 35 (5) (2016) 1182–1195.
[12] M.A. Al-Masni, W.-R. Kim, E.Y. Kim, Y. Noh, D.-H. Kim, A two cascaded network integrating regional-based YOLO and 3D-CNN for cerebral microbleeds detection, in: 2020 42nd Annual International Conference of the IEEE Engineering in Medicine & Biology Society, EMBC, IEEE, 2020, pp. 1055–1058.
[13] S.-Y. Lu, D.R. Nayak, S.-H. Wang, Y.-D. Zhang, A cerebral microbleed diagnosis method via FeatureNet and ensembled randomized neural networks, Appl. Soft Comput. 109 (2021) 107567.
[14] A.L.G. Saint-Esteven, M. Bogowicz, E. Konukoglu, O. Riesterer, P. Balermpas, M. Guckenberger, S. Tanadini-Lang, J.E. van Timmeren, A 2.5 D convolutional neural network for HPV prediction in advanced oropharyngeal cancer, Comput. Biol. Med. 142 (2022) 105215.
[15] H. Zheng, L. Qian, Y. Qin, Y. Gu, J. Yang, Improving the slice interaction of 2.5 D CNN for automatic pancreas segmentation, Med. Phys. 47 (11) (2020) 5543–5554.
[16] Z. Cheng, Y. Bian, S. Fan, Y. Luo, Y. Kang, Automatic detection of cerebral microbleed in SWI images based on 3D CNN, in: BIBE 2019; the Third International Conference on Biological Information and Biomedical Engineering, VDE, 2019, pp. 1–6.
[17] M. Kim, J. Yun, Y. Cho, K. Shin, R. Jang, H.-j. Bae, N. Kim, Deep learning in medical imaging, Neurospine 16 (4) (2019) 657.
[18] J. Wang, H. Zhu, S.-H. Wang, Y.-D. Zhang, A review of deep learning on medical image analysis, Mob. Netw. Appl. 26 (2021) 351–380.
[19] K. Standvoss, T. Crijns, L. Goerke, D. Janssen, S. Kern, T. van Niedek, J. van Vugt, N.A. Burgos, E. Gerritse, J. Mol, et al., Cerebral microbleed detection in traumatic brain injury patients using 3D convolutional neural networks, in: Medical Imaging 2018: Computer-Aided Diagnosis, Vol. 10575, SPIE, 2018, pp. 314–321.
[20] Z. Lu, Y. Yan, S.-H. Wang, CMB-net: a deep convolutional neural network for diagnosis of cerebral microbleeds, Multimedia Tools Appl. 81 (14) (2022) 19195–19214.
[21] Y.-D. Zhang, Y. Zhang, X.-X. Hou, H. Chen, S.-H. Wang, Seven-layer deep neural network based on sparse autoencoder for voxelwise detection of cerebral microbleed, Multimedia Tools Appl. 77 (2018) 10521–10538.
[22] S. Lee, H. Bae, S. Ko, H. Kim, B. Yoon, J. Roh, Comparative analysis of the spatial distribution and severity of cerebral microbleeds and old lacunes, J. Neurol. Neurosurg. Psychiatry 75 (3) (2004) 423–427.
[23] Y.-F. Chen, C.-H. Chen, W.-C. Wu, B.-C. Lee, H.-H. Tsai, S.-C. Tang, Spatial distribution of cerebral microbleeds reveals heterogeneous pathogenesis in CADASIL, Eur. Radiol. (2022) 1–8.
[24] X. Xu, Q.L. Chan, S. Hilal, W.K. Goh, M.K. Ikram, T.Y. Wong, C.-Y. Cheng, C.L.-H. Chen, N. Venketasubramanian, Cerebral microbleeds and neuropsychiatric symptoms in an elderly Asian cohort, J. Neurol. Neurosurg. Psychiatry 88 (1) (2017) 7–11.
[25] J. Fladt, C. Kronlage, G. De Marchis, Cerebral white matter hyperintensities and microbleeds in acute ischemic stroke: impact on recanalization therapies. a review of the literature, Neurosci. Lett. 687 (2018) 55–64.
[26] N. Su, X. Liang, M. Yao, L.-X. Zhou, Q. Wang, Z.-Y. Jin, S.-Y. Zhang, L.-Y. Cui, G. Gong, Y.-C. Zhu, et al., Cerebral microbleeds correlated with white matter and hippocampal volumes in community-dwelling populations, J. Alzheimer's Disease 71 (2) (2019) 559–567.
[27] S.R. Barnes, E.M. Haacke, M. Ayaz, A.S. Boikov, W. Kirsch, D. Kido, Semiautomated detection of cerebral microbleeds in magnetic resonance images, Magn. Reson. Imaging 29 (6) (2011) 844–852.
[28] A. Fazlollahi, F. Meriaudeau, L. Giancardo, V.L. Villemagne, C.C. Rowe, P. Yates, O. Salvado, P. Bourgeat, A.R. Group, et al., Computer-aided detection of cerebral microbleeds in susceptibility-weighted imaging, Comput. Med. Imaging Graph. 46 (2015) 269–276.
[29] T. Li, Y. Zou, P. Bai, S. Li, H. Wang, X. Chen, Z. Meng, Z. Kang, G. Zhou, Detecting cerebral microbleeds via deep learning with features enhancement by reusing ground truth, Comput. Methods Programs Biomed. 204 (2021) 106051.
[30] S. Liu, D. Utriainen, C. Chai, Y. Chen, L. Wang, S.K. Sethi, S. Xia, E.M. Haacke, Cerebral microbleed detection using susceptibility weighted imaging and deep learning, Neuroimage 198 (2019) 271–282.
[31] J. Shi, R. Zhang, L. Guo, L. Gao, H. Ma, J. Wang, Discriminative feature network based on a hierarchical attention mechanism for semantic hippocampus segmentation, IEEE J. Biomed. Health Inf. 25 (2) (2020) 504–513.
[32] Y. Geng, Y. Ren, R. Hou, S. Han, G.D. Rubin, J.Y. Lo, 2.5 D CNN model for detecting lung disease using weak supervision, in: Medical Imaging 2019: Computer-Aided Diagnosis, Vol. 10950, SPIE, 2019, pp. 924–928.
[33] X. Xie, J. Niu, X. Liu, Z. Chen, S. Tang, S. Yu, A survey on incorporating domain knowledge into deep learning for medical image analysis, Med. Image Anal. 69 (2021) 101985.
[34] N. Muralidhar, M.R. Islam, M. Marwah, A. Karpatne, N. Ramakrishnan, Incorporating prior domain knowledge into deep neural networks, in: 2018 IEEE International Conference on Big Data (Big Data), IEEE, 2018, pp. 36–45.
[35] R. Li, C. Yin, S. Yang, B. Qian, P. Zhang, et al., Marrying medical domain knowledge with deep learning on electronic health records: a deep visual analytics approach, J. Med. Int. Res. 22 (9) (2020) e20645.
[36] X. Li, F. Gao, J. Wang, A. Strahler, A priori knowledge accumulation and its application to linear BRDF model inversion, J. Geophys. Res.: Atmos. 106 (D11) (2001) 11925–11935.
[37] L. Liang, P. Zhou, W. Lu, X. Guo, C. Ye, H. Lv, T. Wang, T. Ma, An anatomical knowledge-based MRI deep learning pipeline for white matter hyperintensity quantification associated with cognitive impairment, Comput. Med. Imaging Graph. 89 (2021) 101873.
[38] S. Momeni, A. Fazlollahi, P. Yates, C. Rowe, Y. Gao, A.W.-C. Liew, O. Salvado, Synthetic microbleeds generation for classifier training without ground truth, Comput. Methods Programs Biomed. 207 (2021) 106127.
[39] M.J. Myung, K.M. Lee, H.-G. Kim, J. Oh, J.Y. Lee, I. Shin, E.J. Kim, J. San Lee, Novel approaches to detection of cerebral microbleeds: single deep learning model to achieve a balanced performance, J. Stroke Cerebrovasc. Dis. 30 (9) (2021) 105886.
[40] M.A. Al-Masni, W.-R. Kim, E.Y. Kim, Y. Noh, D.-H. Kim, Automated detection of cerebral microbleeds in MR images: A two-stage deep learning approach, NeuroImage: Clinical 28 (2020) 102464.
[41] B.F. Stanley, S.W. Franklin, Automated cerebral microbleed detection using selective 3D gradient co-occurance matrix and convolutional neural network, Biomed. Signal Process. Control 75 (2022) 103560.
[42] S.M. Smith, M. Jenkinson, M.W. Woolrich, C.F. Beckmann, T.E. Behrens, H. Johansen-Berg, P.R. Bannister, M. De Luca, I. Drobnjak, D.E. Flitney, et al., Advances in functional and structural MR image analysis and implementation as FSL, Neuroimage 23 (2004) S208–S219.
[43] K. Koschmieder, M. Paul, T. van den Heuvel, A. van der Eerden, B. van Ginneken, R. Manniesing, Automated detection of cerebral microbleeds via segmentation in susceptibility-weighted images of patients with traumatic brain injury, NeuroImage: Clinical 35 (2022) 103027.
[44] J. Hong, H. Cheng, S.-H. Wang, J. Liu, Improvement of cerebral microbleeds detection based on discriminative feature learning, Fund. Inform. 168 (2–4) (2019) 231–248.

[45] J. Hong, S.-H. Wang, H. Cheng, J. Liu, Classification of cerebral microbleeds based on fully-optimized convolutional neural network, Multimedia Tools Appl. 79 (21) (2020) 15151–15169.
[46] K.T.M. Han, B. Uyyanonvara, A survey of blob detection algorithms for biomedical images, in: 2016 7th International Conference of Information and Communication Technology for Embedded Systems (IC-ICTES), IEEE, 2016, pp. 57–60.
[47] J. Hong, H. Cheng, Y.-D. Zhang, J. Liu, Detecting cerebral microbleeds with transfer learning, Mach. Vis. Appl. 30 (7) (2019) 1123–1133.
[48] T. Ateeq, M.N. Majeed, S.M. Anwar, M. Maqsood, Z.-u. Rehman, J.W. Lee, K. Muhammad, S. Wang, S.W. Baik, I. Mehmood, Ensemble-classifiers-assisted detection of cerebral microbleeds in brain MRI, Comput. Electr. Eng. 69 (2018) 768–781.
[49] S. Afzal, M. Maqsood, I. Mehmood, M.T. Niaz, S. Seo, An efficient false-positive reduction system for cerebral microbleeds detection, CMC-Comput. Mater. Contin. 66 (2021) 2301–2315.
[50] H. Chen, L. Yu, Q. Dou, L. Shi, V.C. Mok, P.A. Heng, Automatic detection of cerebral microbleeds via deep learning based 3D feature representation, in: 2015 IEEE 12th International Symposium on Biomedical Imaging, ISBI, IEEE, 2015, pp. 764–767.
[51] B. Ghafaryasl, F. van der Lijn, M. Poels, H. Vrooman, M.A. Ikram, W.J. Niessen, A. van der Lugt, M. Vernooij, M. de Bruijne, A computer aided detection system for cerebral microbleeds in brain MRI, in: 2012 9th IEEE International Symposium on Biomedical Imaging, ISBI, IEEE, 2012, pp. 138–141.
[52] M. Dadar, M. Zhernovaia, S. Mahmoud, R. Camicioli, J. Maranzano, S. Duchesne, Using transfer learning for automated microbleed segmentation, bioRxiv (2022) 2022-05.
[53] H. Lee, J.-H. Kim, S. Lee, K.-J. Jung, W.-R. Kim, Y. Noh, E.Y. Kim, K.M. Kang, C.-H. Sohn, D.Y. Lee, et al., Detection of cerebral microbleeds in MR images using a single-stage triplanar ensemble detection network (TPE-det), J. Magn. Reson. Imaging (2022).
[54] Z. Luo, Z. Wang, Y. Huang, L. Wang, T. Tan, E. Zhou, Rethinking the heatmap regression for bottom-up human pose estimation, in: Proceedings of the IEEE/CVF Conference on Computer Vision and Pattern Recognition, 2021, pp. 13264–13273.